Supporting Information:

Plasma-catalytic dry reforming of CH_4: Effects of plasma-generated species on the surface chemistry

Jintao Sun[1], Qi Chen[1]*, Wanyue Qin[1], Hanyu Wu[2], Bowen Liu[2], Shangkun Li[3], Annemie Bogaerts[3]

1. School of Mechanical, Electronic and Control Engineering, Beijing Jiaotong University, Beijing 100044, China

2. College of Chemical Engineering and Environment, China University of Petroleum-Beijing, Beijing 102249, China

3. Research Group PLASMANT, Department of Chemistry, University of Antwerp, Wilrijk 2610, Belgium

*Corresponding author

E-mail address: qchen@bjtu.edu.cn

Section S.1. Preparation and characterization of the catalyst

Silicon dioxide (Aladdin, analytical grade, 20 nm) and $Ni(NO_3)_2{\cdot}6H_2O$ (Aladdin, analytical grade) are used as the support and metal precursor, respectively, to prepare a 10 wt.% Ni/SiO_2 catalyst using the incipient wetness impregnation method. $Ni(NO_3)_2{\cdot}6H_2O$ and the corresponding quantity of SiO_2 (m(Ni):m(SiO_2) = 1:9) are added to deionized water. To fully dissolve the support and precursor, the solution is continuously stirred at 60 ℃ for 2 h and then stirred at room temperature for 12 h. Afterward, the solution is heated to 85 ℃ to evaporate the water until a slurry is formed. After drying by a baking oven at 110 ℃ for 5 h and calcining in a muffle oven at 500 ℃ for 5 h, the sample is reduced with a 0.95 N_2/0.05 H_2 (100 mL/min) mixture at 550 ℃ for 8 h and then sieved to 40-60 mesh. The catalyst is noted as a 10 wt.% Ni/SiO_2 catalyst. The morphology and surface electronic properties of the catalyst are characterized by H_2 temperature-programmed reduction (H_2-TPR, Micromeritics, AutoChem II 2920), X-ray diffraction (XRD, Rigaku, ULTIMA IV, 3 kW), and X-ray photoelectron spectroscopy (XPS, Thermo Fisher Scientific, K-Alpha$^+$, 12 kV).

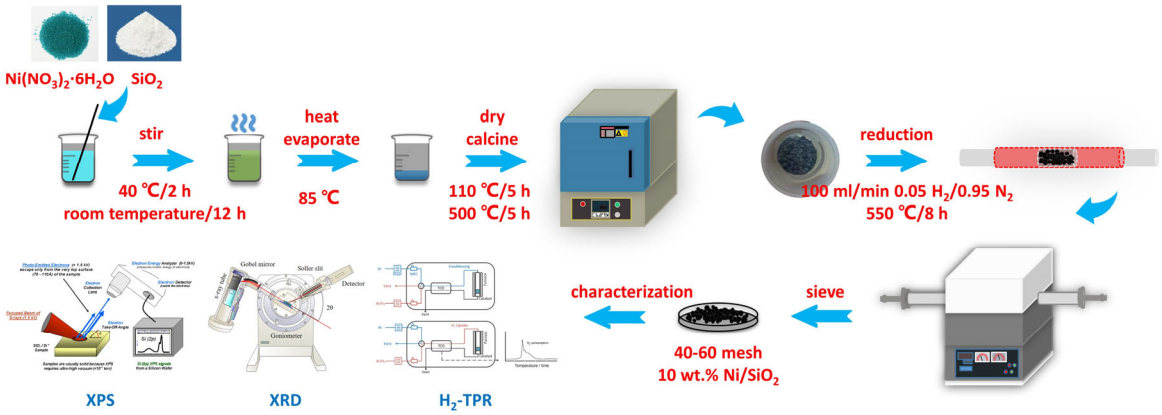

Fig. S1. Schematic diagram of the preparation of Ni/SiO_2 catalyst

To shed light on the distinctive role of the Ni-based catalysts in the plasma-catalytic DRM process, we characterized the Ni/SiO_2 catalyst using XRD, H_2-TPR, and XPS. Fig. S2(a) depicts the XRD spectrum of the Ni/SiO_2 catalyst after H_2 reduction. The diffraction peaks centered at 2θ = 44.43 º, 51.78 º, and 76.26º correspond to the characteristic peaks of metallic Ni, signifying that the loaded metal species predominantly exist on the SiO_2 support surface in the metal state after H_2 reduction. The H_2-TPR profile of the Ni/SiO_2 catalyst prior to thermal

reduction is presented in Fig. S2(b). Two striking reduction peaks within the temperature range of 100-200 ℃ and 350-500 ℃, ascribed to the reduction of bulk NiO (without interaction with SiO_2) and α-phase NiO (weak oxide-support interaction), respectively [1]. The evaluation of H_2-TPR underscores that the Ni/SiO_2 catalyst can be fully reduced under the atmosphere at 550 ℃, which aligns with the XRD analysis.

The XPS spectra for Ni 2p of the Ni/SiO_2 catalyst after reduction are shown in Fig. S2(c). Two peaks are detected with binding energy of 852.76 eV and 869.87 eV, attributed to Ni $2p_{3/2}$ and Ni $2p_{1/2}$ of Ni^0 species, respectively, suggesting the presence of metallic Ni species on the surface of the fresh Ni/SiO_2 catalyst. In addition, peaks appearing at 856.14 eV and 873.57 eV are assigned to Ni^{2+} species. The presence of Ni^{2+} species is further confirmed by the appearance of oscillating satellite peaks at 860.76 eV and 878.62 eV. The XPS results indicate that Ni exists on the surface of Ni/SiO_2 in the form of both Ni^0 and Ni^{2+}, and the proportion of Ni^0 is determined to be 49.6%, which is the primarily active species for the activity in DRM.

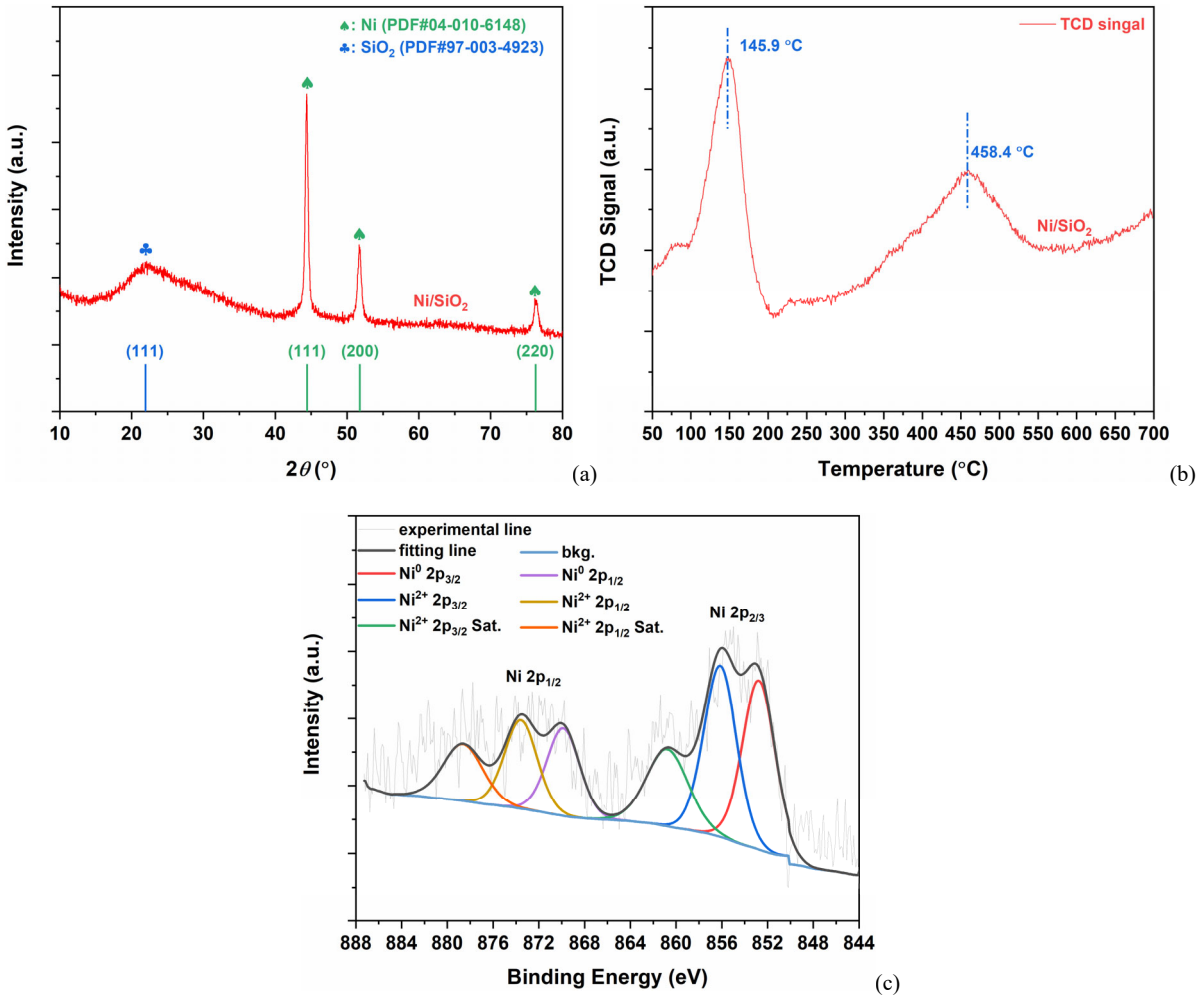

Fig. S2. Characterization of the Ni/SiO_2 catalyst: (a) XRD patterns (after reduction); (b) H_2-TPR profiles (before reduction); (c) Ni 2p XPS spectra (after reduction).

Section S.2. Calculation of reactant conversion and product selectivity

The conversion of CH_4 (X_{CH4}) and CO_2 (X_{CO2}) is defined as [2,3]:

$$X_{CH_4}(\%) = \frac{y_{CH_4}^{in} - \alpha \cdot y_{CH_4}^{out}}{y_{CH_4}^{in}} \times 100\% \quad \text{(S1)}$$

$$X_{CO_2}(\%) = \frac{y_{CO_2}^{in} - \alpha \cdot y_{CO_2}^{out}}{y_{CO_2}^{in}} \times 100\% \quad \text{(S2)}$$

where y_i^{in} and y_i^{out} (i = CH_4, CO_2) are the inlet and outlet reactant mole fractions, respectively. α accounts for the changes in the gas composition and molar flow rate. N_2 is used as an internal standard and added to the gas mixture after the reactor outlet for plasma on and off conditions.

$$\alpha = \frac{y_{plasma}^{off}}{y_{plasma}^{on}} + \beta\left(\frac{y_{plasma}^{off}}{y_{plasma}^{on}} - 1\right) \quad \text{(S3)}$$

Here the factor β is defined as the flow rate of the internal standard with respect to the flow rate at the reactor inlet. The measured ratio $\frac{y_{plasma}^{off}}{y_{plasma}^{on}}$ corresponds to the molar flow changes from chemical reactions while the term '$\beta\left(\frac{y_{plasma}^{off}}{y_{plasma}^{on}} - 1\right)$' accounts for molar flow changes from the dilution.

The selectivity of gaseous products is calculated as [2,3]:

$$S_{CO}(\%) = \frac{\alpha \cdot y_{CO}^{out}}{\left(y_{CH_4}^{in} - \alpha \cdot y_{CH_4}^{out}\right) + \left(y_{CO_2}^{in} - \alpha \cdot y_{CO_2}^{out}\right)} \times 100\% \quad \text{(S4)}$$

$$S_{H_2}(\%) = \frac{2 \cdot \alpha \cdot y_{H_2}^{out}}{4 \cdot \left(y_{CH_4}^{in} - \alpha \cdot y_{CH_4}^{out}\right)} \times 100\% \quad \text{(S5)}$$

$$S_{C_xH_y}(\%) = \frac{x \cdot \alpha \cdot y_{C_xH_y}^{out}}{\left(y_{CH_4}^{in} - \alpha \cdot y_{CH_4}^{out}\right) + \left(y_{CO_2}^{in} - \alpha \cdot y_{CO_2}^{out}\right)} \times 100\% \quad \text{(S6)}$$

Carbon deposition was determined based on thermogravimetric analysis (TGA), and the selectivity of the oxygenates $C_xH_yO_z$ is calculated as:

$$S_{C_xH_yO_z,total}(\%) = 100\% - S_{CO} - S_{C_xH_y} - S_{C_{carbon}} \quad \text{(S7)}$$

$$S_{CH_2O}(\%) = \frac{\alpha \cdot y_{CH_2O}^{out}}{\left(y_{CH_4}^{in} - \alpha \cdot y_{CH_4}^{out}\right) + \left(y_{CO_2}^{in} - \alpha \cdot y_{CO_2}^{out}\right)} \times 100\% \quad \text{(S8)}$$

$$S_{CH_3OH}(\%) = \frac{\alpha \cdot y_{CH_3OH}^{out}}{\left(y_{CH_4}^{in} - \alpha \cdot y_{CH_4}^{out}\right) + \left(y_{CO_2}^{in} - \alpha \cdot y_{CO_2}^{out}\right)} \times 100\% \quad \text{(S9)}$$

The total conversion is defined as the weighted average of the conversion for each reactant, weighted over their concentration in the inlet gas mixture.

$$\chi^{tot} = c_{CH_4} \cdot \chi_{CH_4} + c_{CO_2} \cdot \chi_{CO_2} \quad \text{(S10)}$$

The yields of H_2, CO, hydrocarbons, and oxygenates are defined as:

$$Y_{H_2}(\%) = \frac{\alpha \cdot y_{H_2}^{out}}{2 \cdot y_{CH_4}^{in}} \times 100\% \quad \text{(S11)}$$

$$Y_{CO}(\%) = \frac{\alpha \cdot y_{CO}^{out}}{y_{CH_4}^{in} + y_{CO_2}^{in}} \times 100\% \quad \text{(S12)}$$

$$Y_{C_xH_y}(\%) = \frac{x \cdot \alpha \cdot y_{C_xH_y}^{out}}{y_{CH_4}^{in} + y_{CO_2}^{in}} \times 100\% \quad \text{(S13)}$$

$$Y_{C_xH_yO_z}(\%) = \frac{x \cdot \alpha \cdot y_{C_xH_yO_z}^{out}}{y_{CH_4}^{in} + y_{CO_2}^{in}} \times 100\% \quad \text{(S14)}$$

Section S.3. Total conversion and yields

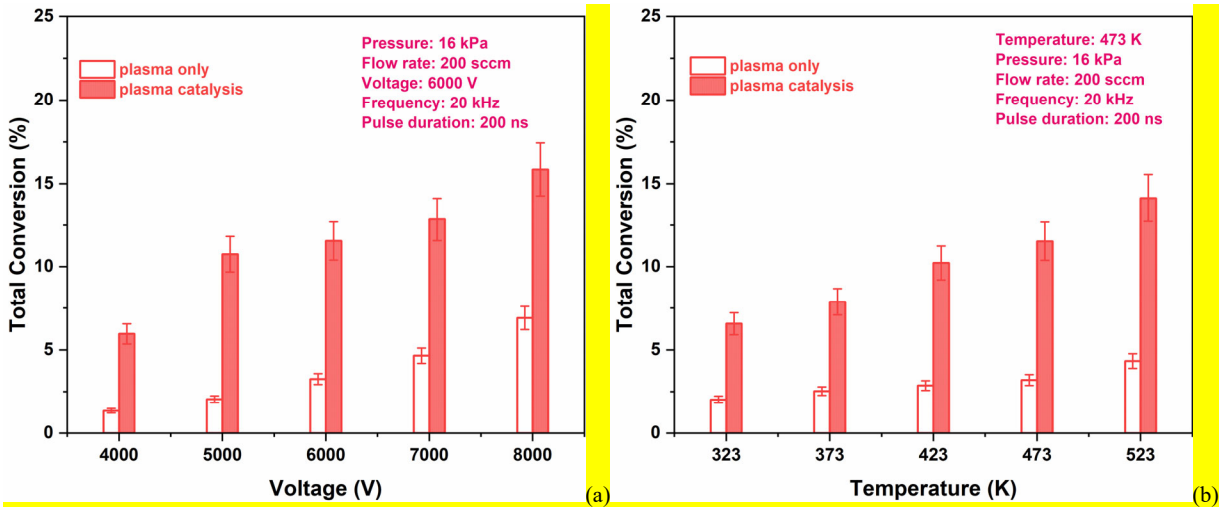

Fig. S3. Experimentally measured total conversion as a function of (a) applied voltage and (b) reaction temperature in plasma-catalytic DRM.

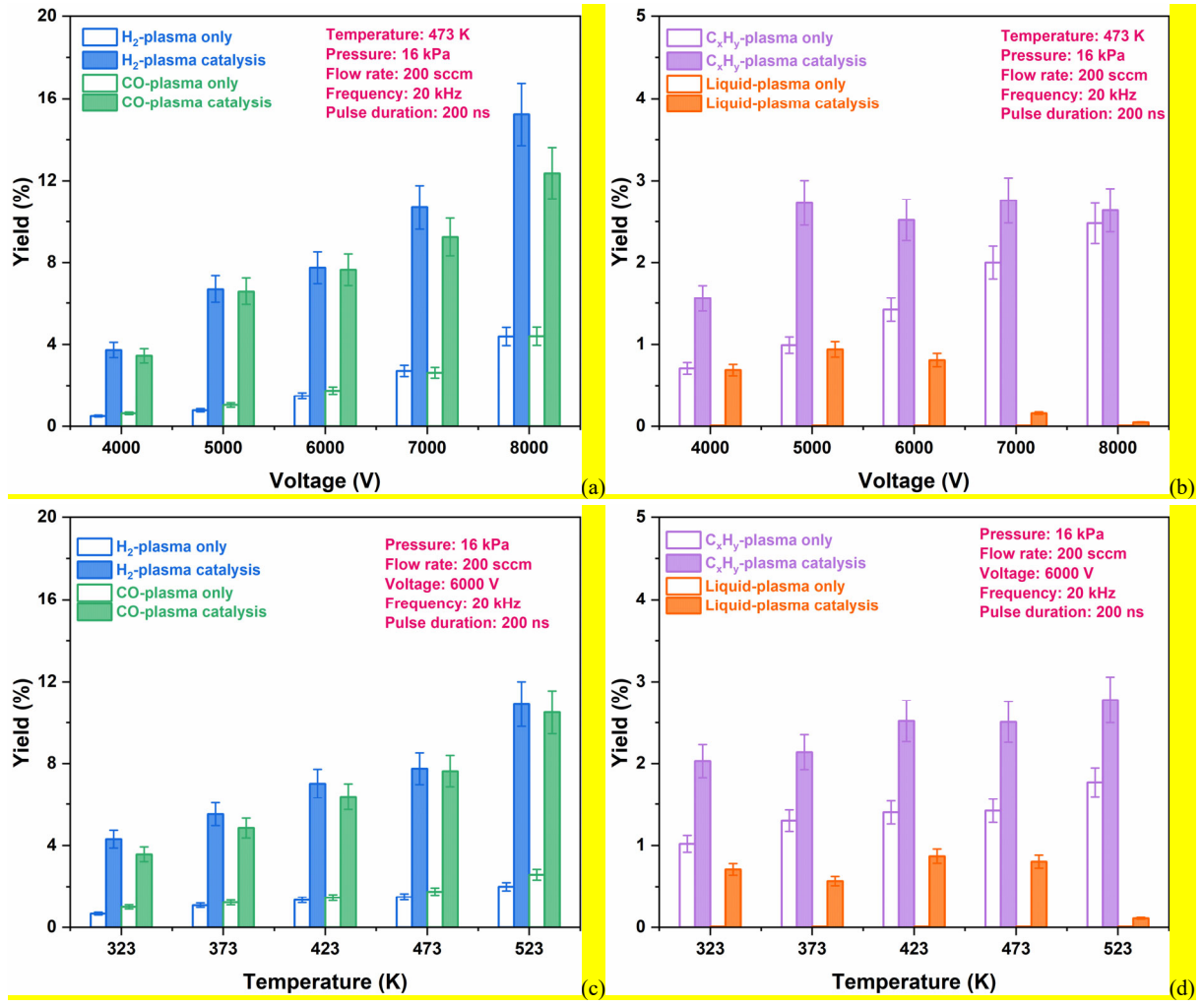

Fig. S4. Effects of applied voltage (a,b) and reaction temperature (c,d) on syngas (a,c) hydrocarbons and oxygenates (b,d) yields.

Section S.4. Optical emission spectra

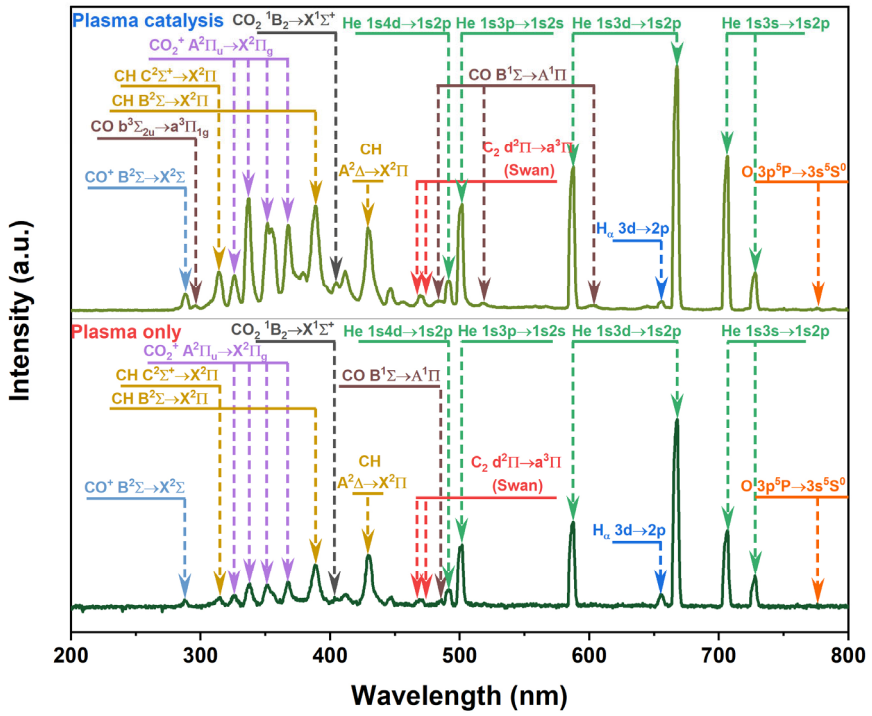

Fig. S5. Optical emission spectra of 0.70 He/0.15 CH_4/0.15 CO_2 plasma: (a) plasma only and (b) packed with Ni/SiO_2 catalyst at applied voltage of 6000 V.

Table S1. Spectroscopic characteristics of the main species detected in the He/CH_4/CO_2 plasma

Species	Electron transition	Wavelength (nm)	Ref.
He	1s4d→1s2p	492	4
	1s3p→1s2s	502	5
	1s3d→1s2p	588	5
		668	5
	1s3s→1s2p	709	5
		728	5
CO_2^+	$A^2\Pi_u \rightarrow X^2\Pi_g$	326	6
		338	6
		351	6
		368	6
CH	$C^2\Sigma^+ \rightarrow X^2\Pi$	314	6
	$B^2\Sigma \rightarrow X^2\Pi$	387	6
	$A^2\Delta \rightarrow X^2\Pi$	431	6
CO	$b^3\Sigma_{2u} \rightarrow a^3\Pi_{1g}$	297	6
	$B^1\Sigma \rightarrow A^1\Pi$	483	6
		519	6
		608	6

CO_2	$^1B_2 \rightarrow X^1\Sigma^+$	403	5
CO^+	$B^2\Sigma \rightarrow X^2\Sigma$	289	6
C_2	$d^2\Pi \rightarrow a^3\Pi$ (Swan band)	468-474	6
O	$3p^5P \rightarrow 3s^5S^0$	777	7
H_α	3d→2p	656	6

Section S.5. Path flux analysis

As the applied voltage and temperature rise, the reduced electric field (*E*/*N*) increases correspondingly, enhancing the electron impact dissociation of CO_2, CH_4, and C_2H_6. This facilitates CO formation while suppressing C_2H_6 formation (see Table S2) and the competitive reaction $CH_4 + CH \rightarrow C_2H_4 + H$ (the dominant C_2H_4 formation pathway, see Fig. S6 and Table S3), leading to reduced hydrocarbons selectivity. On the other hand, the increasing *E*/*N* inhibits the main CH_3OH formation pathways, $O(^1D) + CH_4 \rightarrow CH_3OH$, and the formation of CH_3(s) (the precursor of CH_3OH(s), see Fig. 8), due to the competition with electron impact reactions of CH_4 (see Table S3). Additionally, increasing *E*/*N* leads to a decrease in the electron energy deposited into the CO_2 vibrational excitation channel, thereby reducing HCOOH formation via the catalytic mechanism: CO_2(v) → HCOO(s) → HCOOH(s) → HCOOH (see Fig. 8). Therefore, increasing the applied voltage and temperature lowers the selectivity for oxygenates.

Table S2. C_2H_6 consumption pathways in plasma-catalytic DRM (6000 V, 473 K)

Reaction	Time-integrated reaction rate (mol/cm^3)	Contribution
$e + C_2H_6 \rightarrow e + C_2H_4 + H_2$	2.80×10^{-9}	42.8%
$e + C_2H_6 \rightarrow e + C_2H_5 + H$	9.39×10^{-10}	14.3%
$e + C_2H_6 \rightarrow e + C_2H_2 + H_2 + H_2$	5.65×10^{-10}	8.6%
$e + C_2H_6 \rightarrow e + CH_3 + CH_3$	3.96×10^{-10}	6.1%
$O(^1D) + C_2H_6 \rightarrow C_2H_5OH$	3.86×10^{-10}	5.9%
$e + C_2H_6 \rightarrow e + CH_4 + CH_2$	3.06×10^{-10}	4.7%
$C_2H_6 + OH \rightarrow C_2H_5 + H_2O$	2.97×10^{-10}	4.5%
$O(^1D) + C_2H_6 \rightarrow C_2H_5 + OH$	2.44×10^{-10}	3.7%
$C_2H_6 + CH \rightarrow C_2H_4 + CH_3$	2.41×10^{-10}	3.7%
$e + C_2H_6 \rightarrow e + C_2H_3 + H_2 + H$	9.61×10^{-11}	1.5%
$C_2H_6 + O \rightarrow C_2H_5 + OH$	7.31×10^{-11}	1.1%

Table S3. CH_4 consumption pathways in plasma-catalytic DRM (6000 V, 473 K)

Reaction	Time-integrated reaction rate (mol/cm^3)	Contribution
$e + CH_4 \rightarrow e + CH_4$(v)	7.70×10^{-7}	69.1%
$e + CH_4 \rightarrow e + CH_3 + H$	1.20×10^{-7}	10.8%
$e + CH_4 \rightarrow e + CH_2 + H_2$	5.20×10^{-8}	4.7%
$CH_4 + 2Ni(s) \rightarrow CH_3(s) + H(s)$	5.03×10^{-8}	4.5%
$e + CH_4 \rightarrow e + CH + H_2 + H$	2.30×10^{-8}	2.1%
$CH_4 + CH \rightarrow C_2H_4 + H$	1.95×10^{-8}	1.8%
$e + CH_4 \rightarrow e + C + H_2 + H_2$	1.65×10^{-8}	1.5%
$CH_4^+ + CH_4 \rightarrow CH_5^+ + CH_3$	1.50×10^{-8}	1.4%
$O(^1D) + CH_4 \rightarrow CH_3 + OH$	9.98×10^{-9}	0.9%
$e + CH_4 \rightarrow 2e + CH_4^+$	9.45×10^{-9}	0.8%
$CO_2^+ + CH_4 \rightarrow CH_4^+ + CO_2$	5.09×10^{-9}	0.5%
$CH_3^+ + CH_4 \rightarrow C_2H_5^+ + H_2$	4.81×10^{-9}	0.4%
$e + CH_4 \rightarrow 2e + CH_3^+ + H$	3.55×10^{-9}	0.3%
$O(^1D) + CH_4 \rightarrow CH_3OH$	3.43×10^{-9}	0.3%

$CH_4 + OH \rightarrow CH_3 + H_2O$	3.26×10^{-9}	0.3%
$O(^1D) + CH_4 \rightarrow CH_2OH + H$	2.35×10^{-9}	0.2%

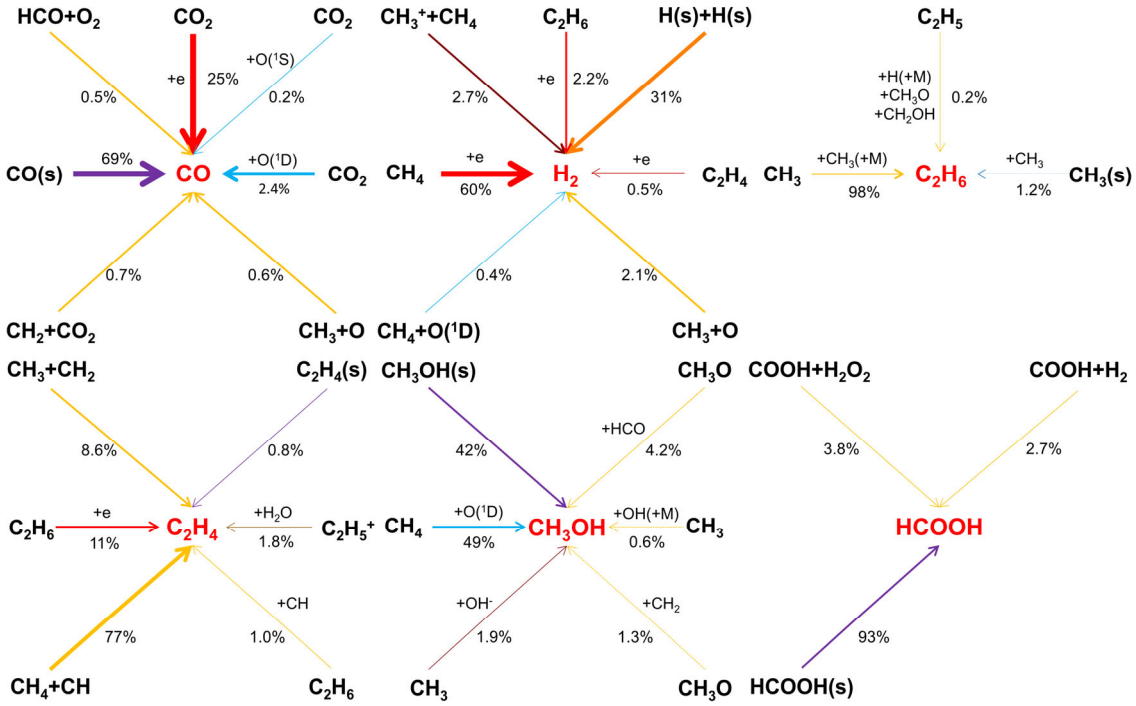

Fig. S6. Reaction path flux analysis for CO, H_2, C_2H_6, C_2H_4, CH_3OH and HCOOH for a 0.15 CH_4/0.15 CO_2/0.70 He mixture at a pressure of 16 kPa, and temperature of 473 K. (red lines: electron impact reactions; yellow lines: chain reactions; light blue lines: chain reactions accelerated by excited species; brown lines: ionic reactions; orange lines: L-H reactions; blue lines: E-R reactions; purple lines: desorption reactions)

Section S.6. Sensitivity analysis

We introduced three additional free energy barriers (0.2 eV, 0.4 eV, 0.6 eV) to the E-R reactions, and the rate constants, $k_{ER,0}$ for E-R reactions with consideration of the enthalpy barrier are calculated with the formula,

$$k_{ER,0} = k_{ER} \exp\left(-E_{ER} / RT\right) \tag{S10}$$

where, k_{ER} is the rate constants for the E-R reactions calculated by eq. (5); and E_{ER} is the assumed additional enthalpy barrier.

To explore the consequences of the assumed E-R rates for these steps on the product concentrations, we calculated the sensitivity coefficient. The definition of logarithmic sensitivity coefficient pS [8] is as follows,

$$pS = \frac{\log\left(Conc'/Conc\right)}{\log\left(k_j'/k_j\right)} \tag{S11}$$

where, k_j' and k_j are the rate coefficients for the jth E-R reaction with and without activation enthalpy considered, respectively. Correspondingly, *Conc'* and *Conc* represent the product concentrations with and without consideration of the activation enthalpy for the jth E-R reaction. Positive and negative values of the sensitivity coefficient indicate the promoting and inhibiting effects for the corresponding E-R reaction on the product formation, respectively.

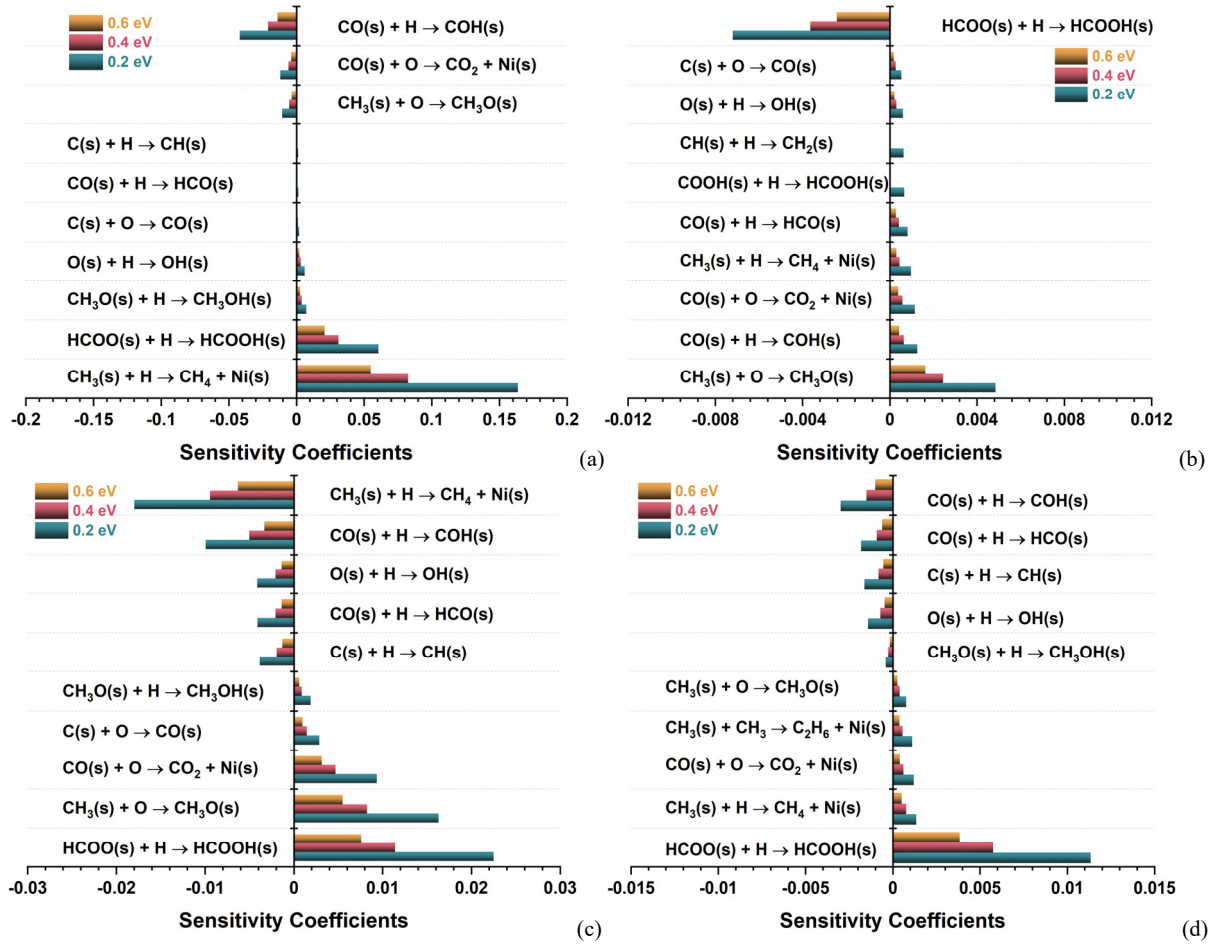

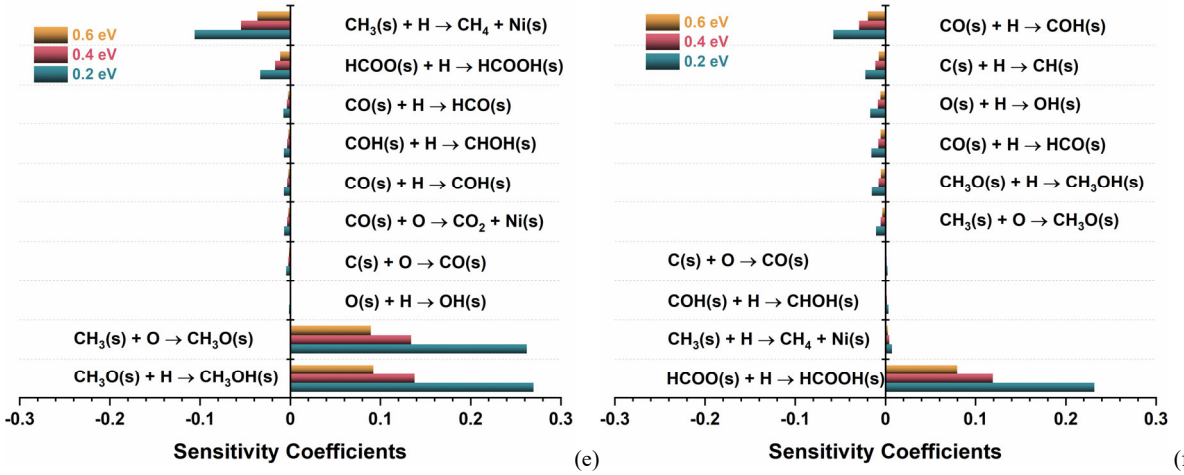

Fig. S7. Sensitivity analysis for (a) CO, (b) H_2, (c) C_2H_4, (d) C_2H_6, (e) CH_3OH and (f) HCOOH formation (CH_4:CO_2:He = 15:15:70; flow rate: 200 sccm; pressure: 16 kPa; reaction temperature: 473 K; applied voltage: 6000 V; discharge frequency: 20 kHz; pulse duration: 200 ns).

Fig. S7(a) shows that the hydrogenation reaction $CH_3(s) + H \rightarrow CH_4 + Ni(s)$ exhibits the most noticeable promoting effect on CO formation. As revealed in Fig. 8, this process is the important pathway for $CH_3(s)$ consumption, leading to the regeneration of active sites Ni(s). This, in turn, promotes the formation of CO(s) through the dehydrogenation of HCO(s), which eventually leads to the production of CO via the desorption of CO(s). Furthermore, the reactions $HCOO(s) + H \rightarrow HCOOH(s)$ and $CH_3O(s) + H \rightarrow CH_3OH(s)$ also present a strong promoting effect on CO production. These processes are also applicable to the similar promotion mechanism, regenerating active sites to promote the L-H reaction $HCO(s) + Ni(s) \rightarrow CO(s) + H(s)$. In contrast, the E-R reaction $CO(s) + H \rightarrow COH(s)$ exhibits the highest negative sensitivity because it is a minor pathway for CO(s) consumption. Meanwhile, another consumption process for CO(s) through the reaction $CO(s) + O \rightarrow CO_2 + Ni(s)$ shows an inhibitory effect on CO production. The strong negative sensitivity of the reaction $CH_3(s) + O \rightarrow CH_3O(s)$ towards CO generation is due to its competition with the E-R reaction $CH_3(s) + H \rightarrow CH_4 + Ni(s)$ for the consumption of $CH_3(s)$.

As illustrated in Fig. S7(b), the oxidation reaction of $CH_3(s)$ with O, yielding $CH_3O(s)$, exhibits the highest positive sensitivity coefficient for the formation of H_2. The produced $CH_3O(s)$ enhances the formation of $CH_3OH(s)$ through the hydrogenation pathway, facilitating the regeneration of active sites Ni(s) due to the relatively low desorption energy of $CH_3OH(s)$ (*ca.* 0.3 eV) [9]. This will promote the formation of H(s) by strengthening the dehydrogenation of CH_4 and further accelerates the L-H reaction $H(s) + H(s) \rightarrow H_2 + 2Ni(s)$. The hydrogenation reaction $CO(s) + H \rightarrow COH(s)$ leads to the formation of COH(s), which, in turn, generates CHOH(s) through further hydrogenation: $COH(s) + H \rightarrow CHOH(s)$. The formed CHOH(s) then promotes the generation of H(s) through the dehydrogenation reaction $CHOH(s) + Ni(s) \rightarrow COH(s) + H(s)$. Additionally, both the oxidative desorption reaction $CO(s) + O \rightarrow CO_2 + Ni(s)$ and the hydrogenation desorption reaction $CH_3(s) + H \rightarrow CH_4 + Ni(s)$ exhibit significant positive sensitivity coefficients due to their ability to promote the regeneration of active sites Ni(s). Fig. S7(b) shows that the hydrogenation reaction $HCOO(s) + H \rightarrow HCOOH(s)$ presents the highest negative sensitivity coefficient. The path flux analysis in Fig. 8 reveals that HCOO(s) is primarily derived from the reaction of vibrationally excited $CO_2(v)$ with H(s). Consequently, the reaction rate of $CO_2(v) + H(s) \rightarrow HCOO(s)$ decreases as the rate of the hydrogenation reaction $HCOO(s) + H \rightarrow HCOOH(s)$ decreases, which ultimately leads to an increase in the concentration of H(s).

The E-R reaction $HCOO(s) + H \rightarrow HCOOH(s)$ has the highest positive sensitivity coefficient for the formation of C_2H_4, as shown in Fig. S7(c). The desorption of HCOOH(s) can promote the regeneration of active

sites Ni(s), further enhancing the generation of $CH_3(s)$ via the dissociative adsorption of CH_4. On one hand, $CH_3(s)$ can recombine to form C_2H_6 via the process $CH_3(s) + CH_3(s) \rightarrow C_2H_6 + 2Ni(s)$. The dissociation of C_2H_6 is the main formation channel of C_2H_4, as shown in Fig. S6 in the SI. On the other hand, $CH_3(s)$ can dehydrogenate on the catalyst surface to form $CH_2(s)$, which accelerates the L-H reaction $CH_2(s) + CH_2(s) \rightarrow C_2H_4(s) + Ni(s)$ and the E-R reaction $CH_2(s) + CH_2 \rightarrow C_2H_4(s)$ to form C_2H_4. Sensitivity analysis shows that the oxidation reactions $C(s) + O \rightarrow CO(s)$, $CO(s) + O \rightarrow CO_2 + Ni(s)$, as well as the formation pathway of $CH_3OH(s)$ via $CH_3(s) + O \rightarrow CH_3O(s)$, $CH_3O(s) + H \rightarrow CH_3OH(s)$ also have relatively high positive sensitivity coefficients, as they can stimulate the regeneration of active sites Ni(s).

The hydrogenation reaction $CH_3(s) + H \rightarrow CH_4 + Ni(s)$ shows the largest negative sensitivity coefficient, indicating that this reaction has the strongest inhibitory effect on the formation of C_2H_4. The consumption pathway analysis of $CH_3(s)$ in Fig. 8 shows that the above-mentioned reaction has a strong competitive relationship with the dehydrogenation of $CH_3(s)$. Therefore, the reaction $CH_3(s) + H \rightarrow CH_4 + Ni(s)$ slows down the process of $CH_2(s) + CH_2(s) \rightarrow C_2H_4(s) + Ni(s)$ and $CH_2(s) + CH_2 \rightarrow C_2H_4(s)$ by inhibiting the formation of $CH_2(s)$. Meanwhile, the E-R reactions $CO(s) + H \rightarrow COH(s)$, $O(s) + H \rightarrow OH(s)$, $CO(s) + H \rightarrow HCO(s)$, $C(s) + H \rightarrow CH(s)$ directly or indirectly inhibit the desorption of CO(s) to regenerate the active sites Ni(s), further suppressing the generation of $CH_2(s)$, as mentioned previously.

Fig. 8 shows that the main formation pathway for $CH_3OH(s)$ is the E-R reaction $CH_3O(s) + H \rightarrow CH_3OH(s)$, while $CH_3O(s)$ is primarily formed through the oxidation reaction $CH_3(s) + O \rightarrow CH_3O(s)$. Therefore, the sensitivity analysis for CH_3OH in Fig. S7(e) indicates a strong positive sensitivity of those two reactions on the generation of CH_3OH. Due to the competition in $CH_3(s)$ consumption by the E-R reaction $CH_3(s) + H \rightarrow CH_4 + Ni(s)$ and $CH_3(s) + O \rightarrow CH_3O(s)$, the E-R reaction $CH_3(s) + H \rightarrow CH_4 + Ni(s)$ suppresses the conversion of $CH_3(s)$ to $CH_3O(s)$, thus inhibiting the formation of $CH_3OH(s)$ and CH_3OH. From Fig. S7(e), it can be observed that the hydrogenation reaction $HCOO(s) + H \rightarrow HCOOH(s)$ also presents a significant negative sensitivity coefficient. The sensitivity analysis for C_2H_6 and HCOOH is also plotted and can be seen in Fig. S7.

In conclusion, Fig. S7 demonstrates that the absolute values of the sensitivity coefficients increase as the activation enthalpy introduced to each E-R reaction decreases, indicating a significant impact on the formation or consumption of each major products. Additionally, the sensitivity coefficients for H_2, C_2H_6, C_2H_4 formation are noticeably smaller compared to those of CO, CH_3OH, and HCOOH. This deviation in the sensitivity coefficients suggests that the influence of E-R reactions on the generation of CO, CH_3OH, and HCOOH is much higher than their promotive effects on the production of H_2, C_2H_6, and C_2H_4, which is verified by the reaction path flux analysis for the aforementioned products in Fig. S6.

Section S.7. Carbon formation mechanism in the gas phase

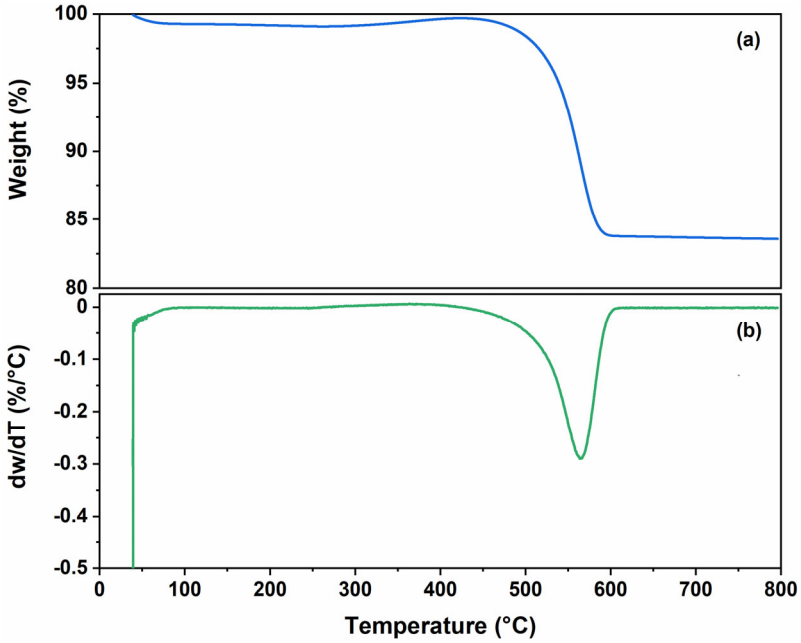

Fig. S8. Analysis of carbon deposition on spent catalysts by (a) TG and (b) DTG profiles.

Thermogravimetric analysis (TGA) was performed to quantify carbon deposition of spent catalysts using a Discovery TGA55 thermogravimetric analyzer (TA, USA). The temperature was increased from 40 to 800 ℃ with a heating rate of 5 ℃/min, in O_2 flow of 100 mL/min. Fig. S8 shows a substantial weight decline of 16.4% for the spent Ni/SiO_2 catalyst. Assuming all Ni was oxidized to nickel oxide during the TG test, the calibrated mass fraction of carbon deposition was determined to be 17.2%, suggesting a large amount of carbon deposition. The carbon species can be divided into amorphous (200~350 ℃), carbon nanotubes (350~700 ℃), and graphitic (> 700 ℃) according to their activity and morphology [10]. From the DTG profile, the Ni/SiO_2 spent catalyst shows one main peak at 564 ℃, suggesting that our deposited carbon mainly exists as carbon nanotubes [10,11].

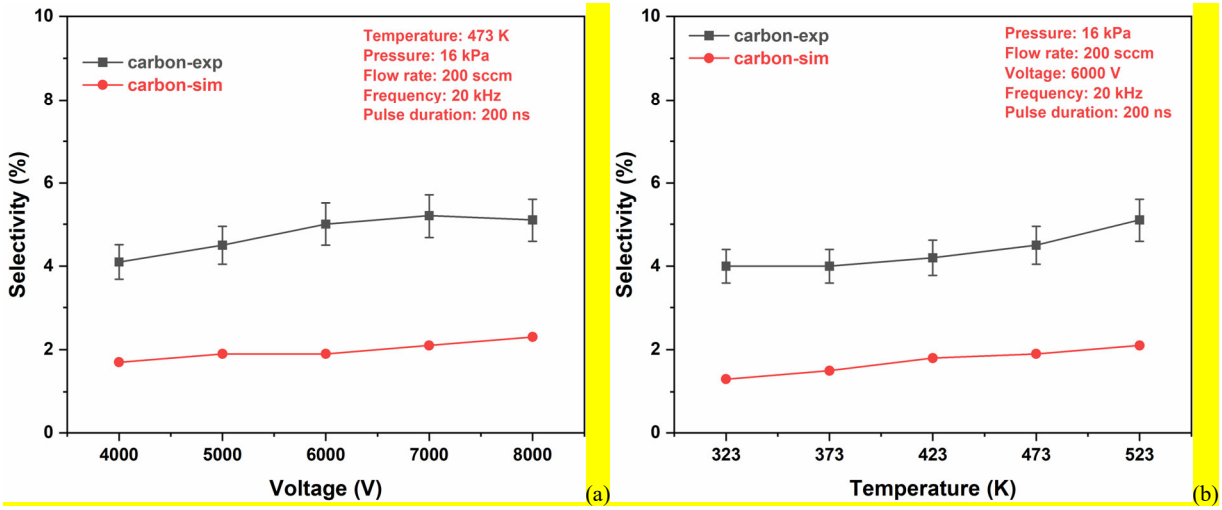

Fig. S9. Comparison of carbon deposition selectivity between experimental measurements and model predictions as a function of (a) applied voltage and (b) reaction temperature in plasma-catalytic DRM.

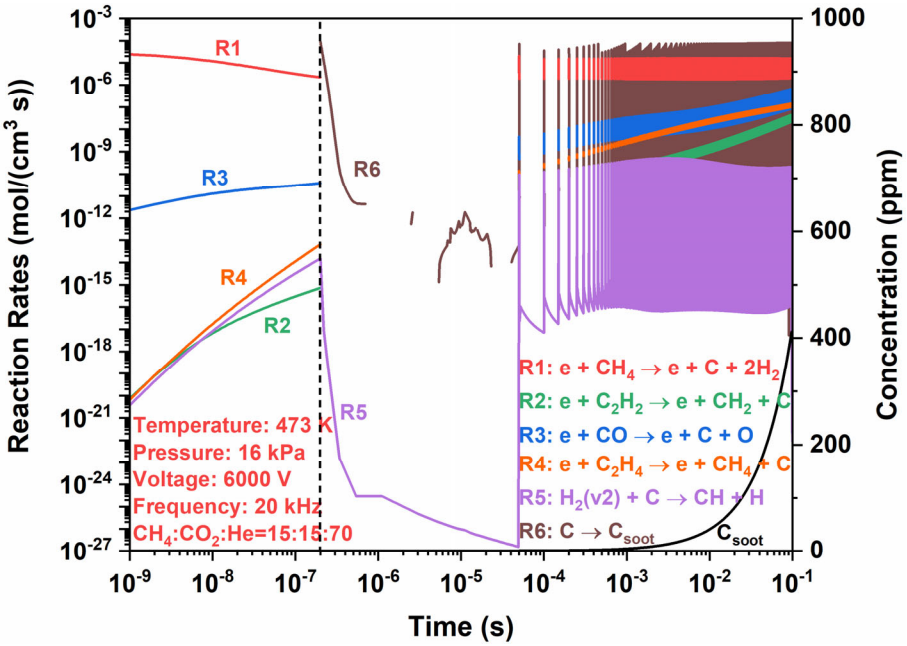

Fig. S10. Time evolution of carbon formation and consumption reactions, as well as carbon concentration, in the gas (plasma) phase, in a 0.15 CH_4/0.15 CO_2/0.70 He mixture at a pressure of 16 kPa, and temperature of 473 K.

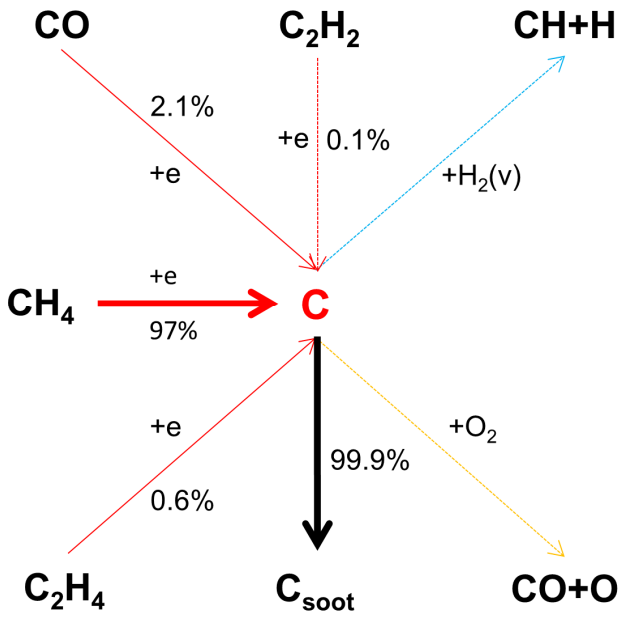

Fig. S11. Path flux analysis for carbon generated in the plasma for a 0.15 CH_4/0.15 CO_2/0.70 He mixture at a pressure of 16 kPa, and temperature of 473 K. (red lines: electron impact reaction; yellow line: chain reaction; light blue line: chain reaction accelerated by excited species; black line: deposition process)

References:

[1] Y. Yi, S. Li, Z. Cui, Y. Hao, et al., Selective oxidation of CH_4 to CH_3OH through plasma catalysis: insights from catalyst characterization and chemical kinetics modelling, *Appl. Catal. B: Environ.* 296 (2021) 120384.
https://doi.org/10.1016/j.apcatb.2021.120384

[2] B. Wanten, R. Vertongen, R. De Meyer, A. Bogaerts, Plasma-based CO_2 conversion: How to correctly analyze the performance? *J. Energy Chem*. 86 (2023) 180-196.
https://doi.org/10.1016/j.jechem.2023.07.005

[3] S. Kelly, E. Mercer, R. De Meyer, R. G. Ciocarlan, S. Bals, A. Bogaerts, Microwave plasma-based dry reforming of methane: Reaction performance and carbon formation, *J. CO_2 Util.* 75 (2023) 102564.
https://doi.org/10.1016/j.jcou.2023.102564

[4] NIST Atomic Spectra Database, https://physics.nist.gov/PhysRefData/ASD/lines_form.html

[5] P.G. Reyes, A. Gómez, J. Vergara, H. Martinez, C. Torres, Plasma diagnostics of glow discharges in mixtures of CO_2 with noble gases, *Rev. Mex. Fis.* 63 (2017) 363-371.

[6] Y. Wang, Y. Chen, J. Harding, H. He, A. Bogaerts, X. Tu, Catalyst-free single-step plasma reforming of CH_4 and CO_2 to higher value oxygenates under ambient conditions, *Chem. Eng. J.* 450 (2022) 137860.
https://doi.org/10.1016/j.cej.2022.137860

[7] L. Dou, Y. Liu, Y. Gao, J. Li, X. Hu, S. Zhang, K. Ostrikov, T. Shao, Disentangling metallic cobalt sites and oxygen vacancy effects in synergistic plasma-catalytic CO2/CH4 conversion into oxygenates, *Appl. Catal. B: Environ.* 318 (2022) 121830.
https://doi.org/10.1016/j.apcatb.2022.121830

[8] J. Sun, Q. Chen, X. Zhao, H. Lin, W. Qin, Kinetic investigation of plasma catalytic synthesis of ammonia: insights into the role of excited states and plasma-enhanced surface chemistry, *Plasma Sources Sci. Technol.* 31 (2022) 094009.
https://doi.org/10.1088/1361-6595/ac8e2c

[9] Y. A. Zhu, D. Chen, X. G. Zhou, W. K. Yuan, DFT studies of dry reforming of methane on Ni catalyst, *Catal. Today* 148 (2008) 260-267.
https://doi.org/10.1016/j.cattod.2009.08.022

[10] Y. Gao, A. Aihemaiti, J. Jiang, Y. Meng, T. Ju, S. Han, X. Chen, J. Liu, Inspection over carbon deposition features of various nickel catalysts during simulated biogas dry reforming, *J. Clean. Prod.* 260 (2020) 120944.
https://doi.org/10.1016/j.jclepro.2020.120944

[11] V. Pawar, D. Ray, C. Subrahmanyam, V. M. Janardhanan, Study of short-term catalyst deactivation due to carbon deposition during biogas dry reforming on supported Ni catalyst, *Energy Fuels* 29 (2015) 8047-8052.
https://doi.org/10.1021/acs.energyfuels.5b01862